ACS OMEGA

Open Access

http://pubs.acs.org/journal/acsodf

Article

Piezoresponse in WO_3 Thin Films Enhanced by Pt-Nanoparticles as Revealed by Atom Probe Tomography and Cs-Transmission Electron Microscopy

Pamela M. Pineda-Domínguez, Torben Boll, Abel Hurtado-Macias, Roberto Talamantes-Soto, John Nogan, Martin Heilmaier,* José Luis Enriquez-Carrejo, Delphine Chassaing, Martin Velazquez-Rizo, Jorge Luis Trimmer-Duarte, Mohana Veerraju Kante, and Manuel Ramos*

Cite This: *ACS Omega* 2025, 10, 17249−17256

Read Online

ACCESS | Metrics & More | Article Recommendations | Supporting Information

ABSTRACT: Tungsten trioxide (WO_3) is an intrinsic *n*-type semiconductor that can be prepared to exhibit a piezoresponse through doping and heat treatment strategies. We report the piezoresponse in platinum-doped WO_3 thin films, prepared by RF/DC cosputtering, followed by postdeposition annealing at 600 °C. Measurements using Switching Spectroscopy Piezo Force Microscopy (SS-PFM) reveal domains with different polarization orientations and hysteresis behavior, corresponding to a piezoelectric coefficient of d_{33} = 97 ± 6 pmV^{-1}. Low-angle x-ray diffraction (XRD) indicates the presence of an orthorhombic structure (β-WO_3) with a *Pbcn* space group, while Scanning Transmission Electron Microscopy (STEM) reveals the formation of platinum nanoparticles (∼5 nm) with a cubic structure ($Fm\bar{3}m$). Atom Probe Tomography (APT) confirms the formation of Pt nanoparticles and Ar-enriched cavities within the WO_3 matrix induced by the annealing process. These structural modifications create lattice strain, giving rise to piezoelectric domains with different polarization orientations.

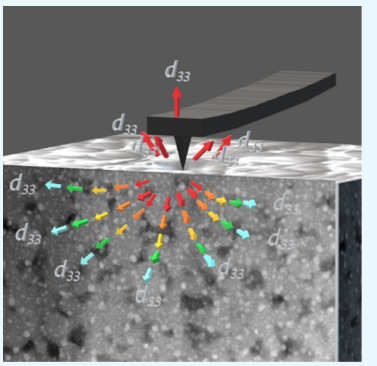

INTRODUCTION

Tungsten trioxide (WO_3) is an *n*-type semiconductor with unique chromogenic, electronic, and catalytic properties. Additionally, it is an environmentally friendly, low-cost, and reliable material used to fabricate several types of sensors, actuators, and power components.[1−3] For example, WO_3 is used as an active layer in electrochromic devices,[4−6] gas sensors,[7,8] and water-splitting devices.[8−12] Doped-WO_3 has been widely studied to improve its photoelectrochemical,[13−15] gasochromic,[7,8] and electrochromic performance.[5,16] Furthermore, the piezoresponse of WO_3 would open an opportunity for diverse applications in the Internet of Things (IoT)[17,18] and microelectromechanical systems (MEMS).[19]

The piezoelectric effect refers to the generation of electric charge in noncentrosymmetric materials when subjected to mechanical strain or stress.[19] The absence of an inversion center in certain crystalline materials leads to the formation of polarized domains due to unbalanced charges. These materials also exhibit the reverse piezoelectric effect in which mechanical deformation is induced by an applied electric field. The reverse piezoelectric effect can be evaluated using switching spectroscopy-piezoresponse force microscopy (SS-PFM) by imaging piezoactive domains and acquiring phase and amplitude hysteresis loops. The SS-PFM signal represents the electromechanical response of the material under an applied bias, which may include several contributions, such as electrostatic effects, electrochemical strain, electrostriction, flexoelectricity, and thermal expansion.

Previous studies have laid the foundation for understanding the origin of the piezoelectric properties in WO_3 thin films. Kim et al. reported a piezoresponse in tungsten trioxide films with a d_{33} coefficient of 7.9 pmV^{-1}, attributed to oxygen-deficient $WO_{2.96}$.[20] Yun et al. determined a lateral piezoresponse of 6 pmV^{-1}, resulting from shear strain gradients at twin walls that induce piezoelectric polarization.[21] We previously reported a d_{33} piezoelectric coefficient of 35 ± 5 pmV^{-1} in WO_3 thin films,[22] attributed to a local break in the crystallographic symmetry due to nanovoid distribution formed during the annealing process.

As-deposited WO_3 films exhibit an amorphous structure, but higher-symmetry crystalline WO_3 phases can be achieved through annealing treatments in the range of 400 to 900 °C, such as triclinic (t), monoclinic (γ), orthorhombic (β), tetragonal (α), and hexagonal (h).[23−25] In addition, to induce crystallization and grain growth,[26,27] annealing also affects the electronic properties of metal oxides by generating zero-

Received: October 10, 2024
Revised: April 6, 2025
Accepted: April 11, 2025
Published: April 25, 2025

https://doi.org/10.1021/acsomega.4c09280
ACS Omega 2025, 10, 17249−17256

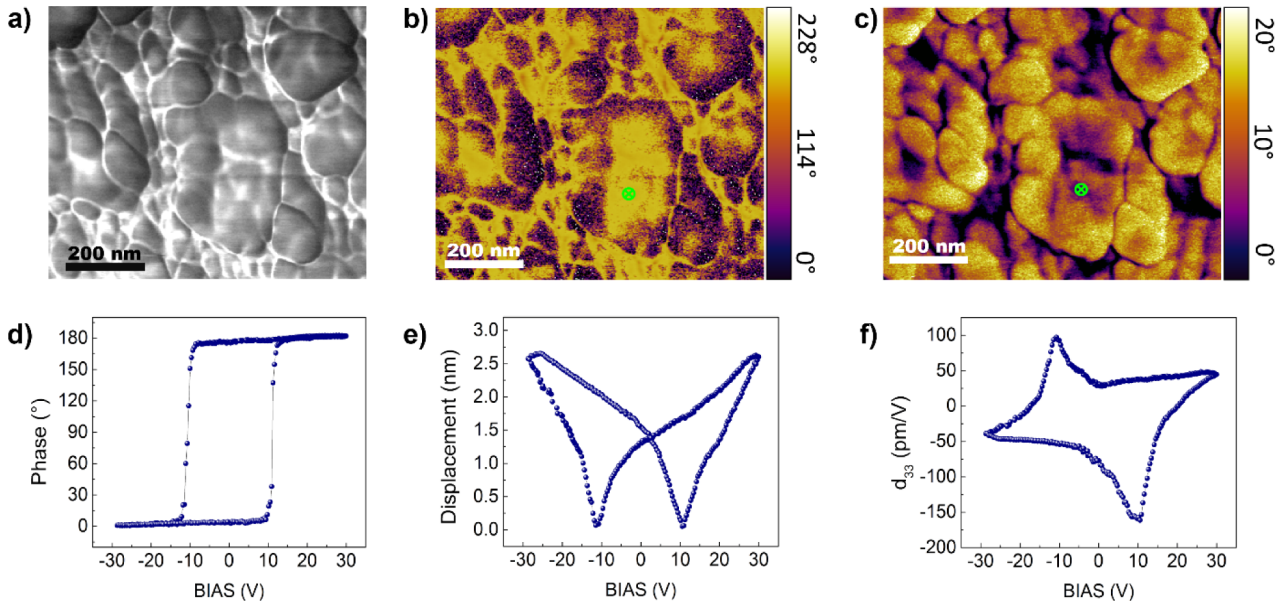

Figure 1. Piezoresponse of the Pt-doped WO_3 film annealed at 600 °C revealed by SS-PFM. (a) Phase signal of the analyzed area. Redistribution of piezodomains (b) before and (c) after measurements. Hysteresis loops of (d) phase and (e) amplitude signals related to (f) piezoelectric coefficient d_{33}.

dimensional point defects, such as oxygen vacancies.[12,28] Other functional defects can be introduced through the incorporation of various kinds of dopants, such as Ti, Li, Pt, and Pd.[5,7,8,29] Among transition metal elements, Pt has a high electron affinity, and its incorporation into the WO_3 matrix can lead to the shifting of the Fermi level toward the valence band (VB), thereby improving electron transport properties.[30] Such heterovalent-ion doping is considered an effective method to improve piezoelectric performance.[31] Size mismatch between different crystalline phases is also known to induce strain, promoting polarization variation.[31] In this context, nanovoids or nanoparticles in the WO_3 lattice may further enhance the piezoresponse by generating inter- and intragrain stress.[22]

While SS-PFM is a commonly used technique for studying piezoresponse at the nanoscale, complementary methods are required to connect it to the nano- and microstructure. X-ray Diffraction (XRD) and Scanning Transmission Electron Microscopy (STEM) are suitable for investigating the crystalline structure, while energy-dispersive spectroscopy (EDS) can be used to determine the Pt distribution. However, analyzing the composition of nanoparticles using STEM/EDS is challenging. In this regard, Atom Probe Tomography (APT) is an outstanding technique for characterizing chemical composition and distribution, particularly for locating dopants and assessing their effects induced by the annealing process.[32−34]

EXPERIMENTAL METHODS

Platinum-doped tungsten trioxide (Pt-doped WO_3) thin films were codeposited using magnetron sputtering technique. High-purity (99.95%) WO_3 and Pt disks were used as targets, and the films were deposited onto SiO_2 substrates with an interlayer of ITO. The base pressure was set to 133.3 Pa before Ar (12 sccm) was allowed into the chamber as the plasma source. The deposition rate was 3 Å/s, at a working pressure of 0.4 Pa, using 225 W of RF power applied to the WO_3 target and 50 W of DC power applied to the Pt target. After deposition, the films were annealed at 400 and 600 °C for 30 min, with a 15 min cooling ramp, under a forming gas atmosphere at a reduced pressure of 3% H_2 in N_2.

Domain imaging and hysteresis loops were obtained using Dual AC Resonance Tracking (DART) and SS-PFM in a commercial Atomic Force Microscope (AFM), model Infinity 3D Asylum Research, equipped with two internal lock-in amplifiers. PFM measurements were performed in a vertical mode using a Pt/Ir conductive tip with an AC voltage amplitude of 5 V_{pk-pk} and a drive frequency of 290 kHz applied between the bottom electrodes. Local polarization was obtained with 5 cycles at an applied voltage from −30 to 30 V. An electrically charged Ag landing electrode was used to diminish electrostatic effects.

The crystallographic structure was determined using XRD on a Panalytical Empyrean system, employing a conventional Cu K_α radiation source (λ=1.54 Å) operating at an accelerating voltage of 40 kV and an emission current of 30 mA. For a scan rate of 20° to 80°, with a step size of 0.05°, XRD patterns were analyzed using HighScore Plus software to determine the crystal structures, average grain size, and average lattice strain.

Before lamella preparation for STEM measurements, the sample was sputter-coated with a 10 nm layer of Au. Lamella lift-out and thinning were performed using an FEI Strata 400S dual-beam system, operated at 30 kV with beam currents ranging from 6.5 nA to 93 pA. Final thinning was conducted at 5 kV with 47 pA to remove surface amorphization. Prior to TEM analysis, the sample holder was introduced into a Fischione Instruments Model 1070 NanoClean plasma cleaner at 60% power for 1 min to remove any organic contaminants resulting from sample transfer and handling. STEM measurements were carried out using double Cs-corrected Titan Themis Z (Thermo Fisher Scientific), operated at an accelerating voltage of 300 kV and a beam current of 0.80 pA. The analysis included STEM imaging with a semi-convergence angle of 30 mrad, and all images were acquired in a high-angle annular dark-field (HAADF) mode. Additionally, EDS analysis was performed under the same imaging and operating conditions. The Inorganic Crystal Structure Data-

https://doi.org/10.1021/acsomega.4c09280
ACS Omega 2025, 10, 17249−17256

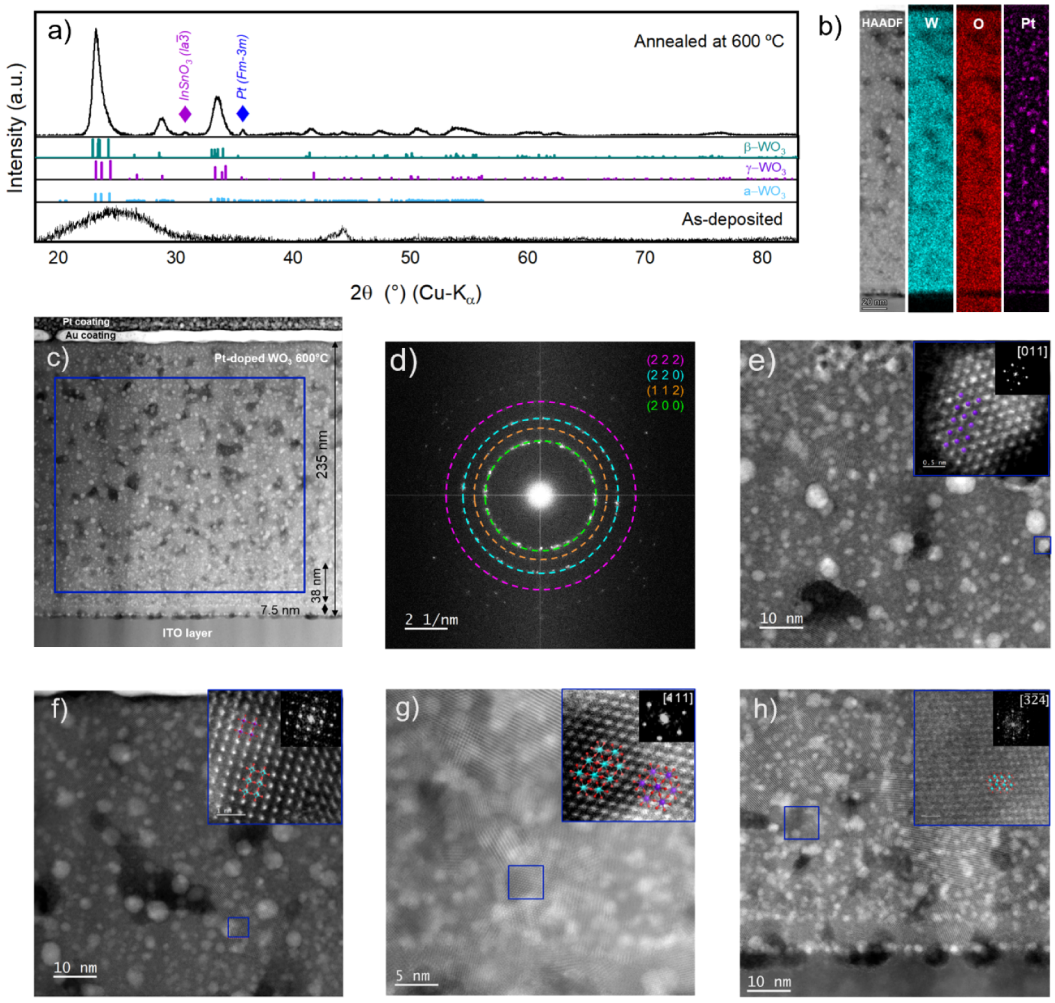

Figure 2. (a) Low angle X-ray diffraction pattern for the cosputtered Pt-doped WO_3 thin film annealed at 600 °C under 3% H_2/N_2 forming gas environment. Comparison with anorthic (a), monoclinic (γ), and orthorhombic (β) WO_3 structures. (b) EDS for W, O, and Pt. (c) HAADF STEM image of the Pt-doped WO_3 thin film annealed at 600 °C onto the ITO layer. (d) FFT focused on the blue-squared region showing the polycrystalline diffraction pattern of a β-WO_3 structure (mp-2383161). (e) HAADF-STEM images of corresponding FFTs in zone axes [100], (f) [111], and (g) [324] corresponding to a β-WO_3 structure. (h) FFT in the zone axis [011], corresponding to the metallic Pt cubic structure.

base (ICSD) and Materials Project (mp) databases were used for the comparison of the measured d-spacings.

The APT tips were prepared using a lift-out process and annular milling with a focused ion beam (FIB) in a scanning electron microscope, a model Zeiss Auriga. To avoid beam-induced amorphization, a Pt coating was deposited on the film surface. The three-dimensional distribution for W, O, and Pt was obtained with a Cameca LEAP 4000X high-resolution system equipped with a UV laser ($\lambda \sim 355$ nm). APT measurements for the as-deposited samples and those annealed at 600 °C were performed at a temperature set to 50 K, with a detection rate of 0.3%, a pulse rate of 100 kHz, and a laser pulse energy of 30 pJ. All APT data were reconstructed with Cameca AP Suite 6.3. Mass calibration was performed using Si, Ar, In, Sn, Pt, and W oxides while avoiding overlapping peaks. The reconstructions were cropped to cylinders 130 nm in length and 20 nm from the interface with the ITO layer. The difference in shape of the analyzed cylinders for the as-deposited film and annealed at 600 °C is related to the sample preparation. However, the data set for analysis is comparable. Nearest Neighbor Distributions (NNDs) for Ar and Pt were calculated for the second-order nearest neighbors, with a maximum pair distance of 3 nm and a sample width of 0.1 nm. Radial distribution functions were calculated for a maximum distance of 4 nm and 0.1 bin width.

RESULTS

The topography of the Pt-doped WO_3 film annealed at 600 °C is displayed in Figure 1a. SS-PFM imaging of the same region shows the redistribution of a piezodomain under an applied bias before (Figure 1b) and after (Figure 1c) measurement, revealing the reorientation of polarization with the applied field. This is characterized by a phase shift from positive polarization domains (white regions) to in-plane polarizations (violet regions) and remnant polarization (yellow regions).[35] Accordingly, the piezoresponse is confirmed by the hysteresis loops of phase and amplitude presented in Figure 1d,e, respectively. The phase signal shows a 180° shift, and a coercive voltage of 30 V is obtained by using the relation $V_c = (V_c^+ - V_c^-)/2$, where V_c^+ and V_c^- are forward and reverse coercive bias voltages, respectively. The amplitude signal shows a maximum displacement of 2.5 nm with an applied bias of 30 V. In this case, the hysteresis loops are centered with respect to the applied bias and exhibit a symmetric shape.[36] The local d_{33}

https://doi.org/10.1021/acsomega.4c09280
ACS Omega 2025, 10, 17249−17256

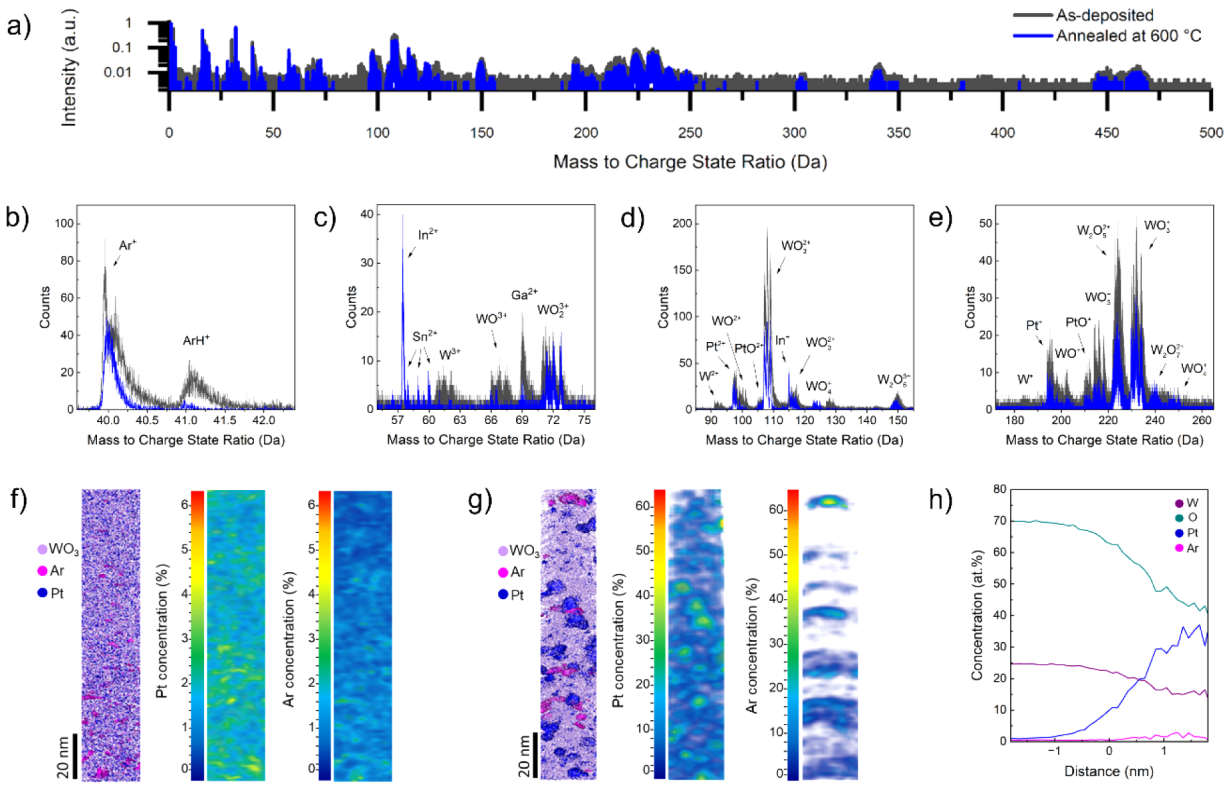

Figure 3. (a) Complete APT mass spectrum for as-deposited Pt-doped WO_3 and annealed at 600 °C acquired. (b)−(e) APT mass spectrum from regions with relevant overlaps. Tomography and heat maps of Ar and Pt atomic concentration for selected cylinders of Pt-doped WO_3 thin films (f) without and (g) with postdeposition annealing treatment of 600 °C under 3% H_2/N_2. (h) Proxigram for the Pt-nanoparticles isosurface. For the sample without annealing Pt and Ar concentration, isosurface values are 3 atom % Ar and 5 atom % Pt. For the sample annealed at 600 °C, they are 9 at. % Ar and 17 at. % Pt.

is estimated using the relation $d_{33} = (D - D_1)/(V - V_1)$, where D is the piezoelectric deformation (or amplitude) and V is the applied voltage, with D_1, and V_1 representing the values at the intersection of the butterfly hysteresis loop. These results indicate a piezoelectric behavior with an estimated d_{33} coefficient of 97 ± 6 pmV^{-1}, where the margin of error refers to the oscillation of the $d_{33,max}$ coefficient during the 5-cycle measurement. Therefore, it can be concluded that Pt-doping in WO_3 enhances the piezoelectric coefficient, compared to our previously reported value of 35 ± 5 pmV^{-1} for WO_3 thin films.[22] Structural analysis by XRD confirms an amorphous structure for the as-deposited film and reveals a crystalline structure after annealing at 600 °C. The diffraction pattern in Figure 2a shows principal diffraction planes at 23.3°, 29°, and 33.8°, which can be matched to an anorthic (a), monoclinic (γ), or orthorhombic (β) WO_3 structure, according to the Powder Diffraction File (PDF): 96-210-6294, 96-152-7083, and 96-210-7313, respectively. The main diffraction planes of the ITO layer and Pt can also be identified at 30.2° and 41°, respectively. Additionally, the peaks around 62° and 75° can be attributed to γ and β phases of WO_3. The Scherrer method was used to calculate an average crystallite size of 14 nm.[37]

The HAADF-STEM image in Figure 2c reveals the film's microstructure, showing Pt nanoparticles (bright contrast) ranging from 4 to 6 nm, along with lower-density regions (dark contrast) between 5 and 15 nm within the WO_3 lattice. The Fast Fourier Transformation (FFT) presented in Figure 2d corresponds to a polycrystalline diffraction pattern for this region. EDS elemental mapping in Figure 2b displays the distribution of W and O, highlighting low-density regions in the oxide matrix as well as the distribution of Pt nanoparticles. Figure 2e−h shows different in-axis zones used to measure the d-spacing between observable atomic planes. Three different in-axis orientations of the WO_3 structure with respect to the electron beam were observed as follows: (e) near the film surface, in-axis with [100]; (f) in the middle of the film thickness, in-axis with [111]; and (g) near the ITO layer, in-axis with [$\underline{3}24$]. The d-spacings of the triclinic and monoclinic WO_3 structures suggested by XRD results differed significantly and were therefore not considered for comparison. The measured d-spacings can be attributed to either a cubic structure (*Pm-3m*, ICSD: 01-074-6028) with planes (001), (011), and (010) or to an orthorhombic structure (*Pbcn*, mp-2383161) with planes (002), (022), and (020). In the polycrystalline pattern in Figure 2c, the diffraction rings can be assigned to (100), (110), and (111) of a cubic structure or to (200), (220), and (222) of an orthorhombic structure. Although the β-WO_3 structure is typically expected at an annealing temperature of 600 °C, cubic structures for Pt-doped WO_3 have also been extensively reported in the literature.[38−40] However, the orange diffraction ring in Figure 2c can only be assigned to the (112) plane of a β-WO_3 structure, suggesting that this phase is present. The structure of the Pt nanoparticles is identified as cubic[35] ($Fm\bar{3}m$, 01−085−5676) based on the in-axis zone oriented with [011], as shown in Figure 2h. The measured d-spacings 2.3, 1.41, 2.34, and 1.98 Å correspond to the planes (1 −1 1), (0 −2 2), (−1 −1 1), and (−200), respectively. The formation of Pt nanoparticles supported within a WO_3 matrix after heat treatments at 600 °C has been

https://doi.org/10.1021/acsomega.4c09280
ACS Omega 2025, 10, 17249−17256

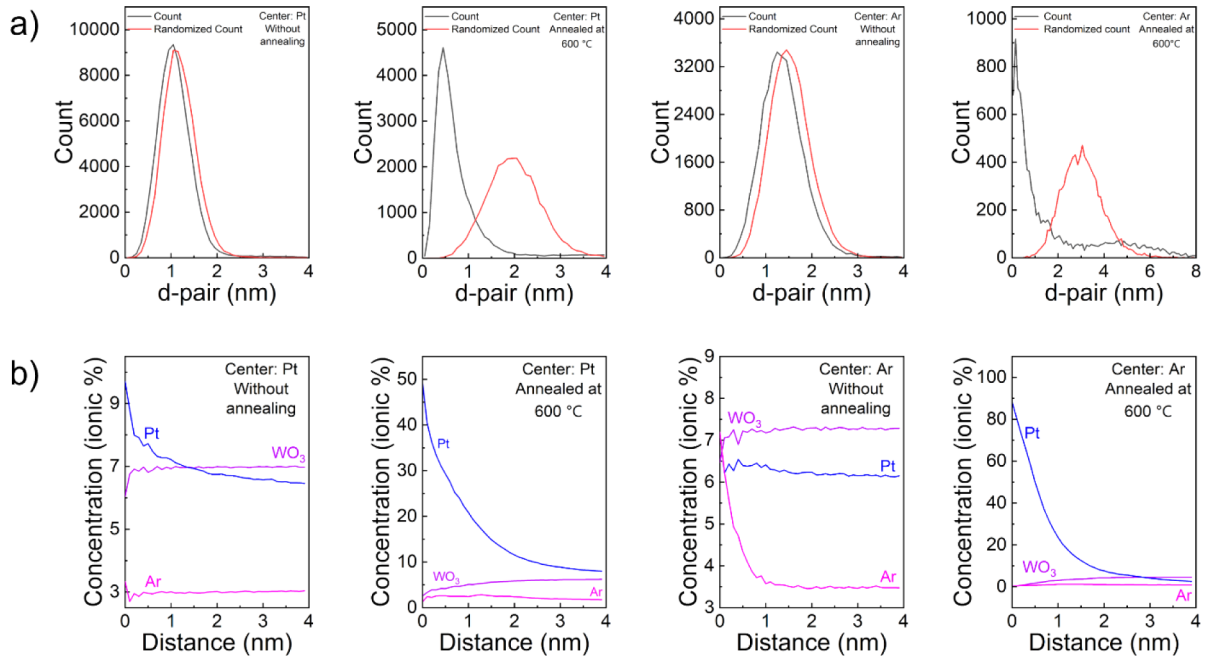

Figure 4. (a) Second-order nearest neighbor distribution (NND) and (b) radial distribution function (RDF) of Pt-doped WO_3 thin films as-deposited and annealed at 600 °C, with Ar and Pt ions as centers for the calculations.

achieved by others, independently of the synthesis method, and is confirmed in our study.[34,35]

To investigate the three-dimensional chemical distribution at the nanoscale, APT was performed on both the as-deposited film and the film annealed at 600 °C; the comparison of the acquired mass spectra is displayed in Figure 3a (a larger image is provided in Supporting Information S1). The as-deposited sample exhibits a larger ArH^+ peak in the mass-to-charge-ratio spectrum, at approximately 41 Da, compared to the annealed sample (Figure 3b). The complex mass spectra acquired contain several overlapping peaks, which are excluded from the ion maps displayed in Figure 3b–e. The main overlaps occur for Pt and W oxide species in Figure 3c: Pt^{2+}/WO^{2+} (at 99 Da), PtO^{2+}/WO_2^{2+} (at 106 Da, 106.5 Da, 107 Da), and In^+/WO_3^{2+} (115 Da), and in Figure 3d–h: Pt^+/WO^+ (198 Da) and WO_2^+/PtO^+ (214 Da). A more detailed list of overlapping peaks is provided in Supporting Information S2 and S3 as tungsten oxide, such as other metal oxides, has been reported to evaporate into complex molecules (W_nO_m).[41] Additionally, Raman spectroscopy results presented in Supporting Information S4 show no evidence of Pt–W or Pt–O vibrational modes near the thin film surface, with the main vibration modes confirming only the presence of the WO_3 structure.

The atomic concentration of Pt, obtained by decomposition of peaks considering overlaps, is 2.2 at. % in the as-deposited film and increases to 5.2 at. % after annealing. In the as-deposited sample, metallic Pt species (Pt^+, Pt^{2+}) are homogeneously distributed, whereas in the annealed film, Pt forms nanoparticles ranging from 4 to 6 nm. This distribution is visualized in Figure 3g, where Pt is delineated by concentration isosurfaces. A detailed analysis of the Pt nanoparticles' chemical composition using a proxigram (Figure 3h) reveals a correlation with Ar-enrichment near the nanoparticles. The maximum level of Pt does not reach 100%, which can be attributed to ion scattering artifacts in the APT. STEM results confirm that the Pt nanoparticles in the annealed films possess a crystalline structure corresponding to pure Pt. In both samples, Pt-oxide species (PtO^+, PtO^{2+}) are homogeneously distributed, indicating that while some Pt forms nanoparticles, a portion remains dissolved in the WO_3 phase as a solid solution rather than fully clustering. The tomography of the as-deposited sample reveals Ar-clustering near the substrate (Figure 3g) corresponding to the low-density regions observed in STEM. These regions are identified as Ar-clusters (10–15 nm in size), which can be interpreted as cavities filled with Ar during the deposition process. The plate-like shape of these Ar-clusters is attributed to the rapid evaporation of gas upon reaching the cavity, as previously reported.[22] To quantitatively analyze clustering, radial distribution functions (RDFs) and Nearest Neighbor Analysis (NNA)[37] were employed. In Figure 4a, NNA for the second nearest neighbor of either the Pt-species or Ar^+/ArH^+ shows that after annealing, the distance between peaks random for the experimental distribution increases compared to the as-deposited sample. This indicates that heat treatment enhances ordering or the degree of clustering. The RDF analysis in Figure 4b further confirms this clustering process, revealing that while Pt and Ar were initially uncorrelated, they became correlated after annealing. Additionally, APT exposes In-diffusion from the ITO layer into the WO_3 film after annealing, forming a concentration gradient extending up to 40 nm into the film.

DISCUSSION

Based on our comprehensive study of WO_3 thin films using XRD, Cs-corrected STEM, and Atom Probe Tomography (APT), we propose several possible mechanisms contributing to the observed enhancement in piezoresponse. These mechanisms include (a) indium (In) diffusion from the ITO, (b) substitutional Pt-doping in the WO_3 matrix and formation of Pt-nanoparticles due to postdeposition annealing at 600 °C, and (c) the presence of nanocavities within the WO_3 matrix. While engineering nanocrystallinity is known to enhance the PFM response,[42] our previous studies[22] have demonstrated

https://doi.org/10.1021/acsomega.4c09280
ACS Omega 2025, 10, 17249−17256

that strong crystallinity alone is insufficient to induce high d_{33} values, suggesting that additional factors are at play. To assess the role of indium (In) diffusion, we compared our results to previous work, where a PFM response was observed in samples fabricated without an ITO layer. This suggests that In-diffusion is not the primary factor responsible for the observed piezoresponse enhancement. Another important aspect is Pt-doping in the WO_3 matrix. While Pt is known to modify the WO_3 band structure,[30] potentially influencing the piezoresponse, an additional contributing mechanism involves the formation of oxygen vacancies in an H-rich environment. This process is similar to the findings of Li et al.,[11] who studied the photocatalytic properties of the material. In their work, exposure to $NaBH_4$ provided hydrogen to the system, facilitating diffusion of H into the WO_3 matrix. In our case, annealing in forming gas introduces hydrogen into the material. This H readily diffuses into the WO_3 matrix, where it interacts with tetravalent Pt ions, reducing Pt^{4+} to metallic Pt. As a result, electrons are transferred from H atoms to O atoms in the lattice, producing a high concentration of oxygen vacancies within the lattice, which are known to play a crucial role in enhancing piezoelectric properties.[31] Beyond modifications to electronic properties, strain also contributes to the enhancement of the piezoresponse. In addition to Pt doping and oxygen vacancy formation, as previously discussed, strain can be introduced by alteration of the nanostructure. While the effect of nanocavities on piezoresponse has been previously studied,[22,42] this work also reveals the presence of Pt-nanoparticles. These Pt nanoparticles can induce localized strain in the material, which, in turn, enhances the piezoresponse measured by SS-PFM.[43]

CONCLUSIONS

Pt-doped WO_3 thin films prepared via cosputtering (RF/DC) technique followed by postdeposition annealing at 600 °C exhibited a significant local piezoresponse, as measured by SS-PFM, with a piezoelectric coefficient $d_{33} = 97 \pm 6$ pmV^{-1}. The piezoresponse was characterized by a 180° phase-shift hysteresis loop and 2.5 nm of displacement in the amplitude hysteresis loop. Low-angle XRD analysis revealed an amorphous structure for the as-deposited film and a crystalline WO_3 phase for the annealed film. STEM confirmed the formation of an orthorhombic β-WO_3 phase with (020) and (202) diffraction planes for the annealed samples. Additionally, STEM revealed nanocavities (10−20 nm) within the tungsten oxide matrix, as well as Pt-nanoparticles (4−6 nm) distribution. APT analysis provided a three-dimensional chemical distribution, confirming the formation of Pt-nanoparticles and Ar-filled cavities formed during annealing at 600 °C. These features likely act as stress centers, inducing strain and deformation in the WO_3 lattice, which may contribute to the formation of localized piezoelectric domains with varying polarization orientations.

ASSOCIATED CONTENT

Supporting Information

The Supporting Information is available free of charge at https://pubs.acs.org/doi/10.1021/acsomega.4c09280.

S1: Comparison of APT mass spectra for as-deposited Pt-doped WO_3 and annealed at 600 °C; S2: APT mass spectrum for as-deposited Pt-doped WO_3 and annealed at 600 °C showing the regions of interest with tungsten oxide ion species, such as WO, WO_2, WO_3, W_2O_5, and W_2O_7, as well as Pt-species and In and Sn from the ITO; S3: the list of overlapping peaks acquired by APT; S4: Raman spectroscopy analysis (PDF)

AUTHOR INFORMATION

Corresponding Authors

Manuel Ramos − *Departamento de Física y Matemáticas, Instituto de Ingeniería y Tecnología, Universidad Autónoma de Cd. Juárez, Cd. Juárez, Chihuahua 32310, Mexico;* orcid.org/0000-0002-1781-054X; Email: manuel.ramos@uacj.mx

Martin Heilmaier − *Institut für Angewandte Materialien-Werkstoffkunde (IAM-WK), Karlsruhe Institute of Technology, Karlsruhe 76131, Germany;* Email: martin.heilmaier@kit.edu

Authors

Pamela M. Pineda-Domínguez − *Institut für Angewandte Materialien-Werkstoffkunde (IAM-WK), Karlsruhe Institute of Technology, Karlsruhe 76131, Germany*

Torben Boll − *Institut für Angewandte Materialien-Werkstoffkunde (IAM-WK), Karlsruhe Institute of Technology, Karlsruhe 76131, Germany; Karlsruhe Nano Micro Facility (KNMFi), Karlsruhe Institute of Technology (KIT), Eggenstein-Leopoldshafen 76344, Germany; Institute for Nanotechnology (INT), Karlsruhe Institute of Technology (KIT), Eggenstein-Leopoldshafen 76344, Germany*

Abel Hurtado-Macias − *Laboratorio Nacional de Nanotecnología, Centro de Investigación en Materiales Avanzados SC, Chihuahua 31109, Mexico*

Roberto Talamantes-Soto − *Laboratorio Nacional de Nanotecnología, Centro de Investigación en Materiales Avanzados SC, Chihuahua 31109, Mexico*

John Nogan − *Center for Integrated Nanotechnologies, Albuquerque, New Mexico 87110, United States*

José Luis Enriquez-Carrejo − *Departamento de Física y Matemáticas, Instituto de Ingeniería y Tecnología, Universidad Autónoma de Cd. Juárez, Cd. Juárez, Chihuahua 32310, Mexico*

Delphine Chassaing − *Institut für Angewandte Materialien-Werkstoffkunde (IAM-WK), Karlsruhe Institute of Technology, Karlsruhe 76131, Germany; Karlsruhe Nano Micro Facility (KNMFi), Karlsruhe Institute of Technology (KIT), Eggenstein-Leopoldshafen 76344, Germany*

Martin Velazquez-Rizo − *Karlsruhe Nano Micro Facility (KNMFi), Karlsruhe Institute of Technology (KIT), Eggenstein-Leopoldshafen 76344, Germany; Institute for Nanotechnology (INT), Karlsruhe Institute of Technology (KIT), Eggenstein-Leopoldshafen 76344, Germany*

Jorge Luis Trimmer-Duarte − *Departamento de Física y Matemáticas, Instituto de Ingeniería y Tecnología, Universidad Autónoma de Cd. Juárez, Cd. Juárez, Chihuahua 32310, Mexico*

Mohana Veerraju Kante − *Institute for Nanotechnology (INT), Karlsruhe Institute of Technology (KIT), Eggenstein-Leopoldshafen 76344, Germany*

Complete contact information is available at: https://pubs.acs.org/10.1021/acsomega.4c09280

https://doi.org/10.1021/acsomega.4c09280
ACS Omega 2025, 10, 17249−17256

Author Contributions

Sample preparation was carried out by P.M.P.-D., J.N., and M.R.; PFM measurements were performed by A.H.-M and R.P.T.S.; XRD measurements were performed by K.M.V; STEM was completed by M.V.R. and J.T.; Raman spectroscopy measurements were performed by J.L.E.-C; APT sample preparation and measurements were completed by DC; APT analysis was completed by P.M.P.D. and T.B.; original draft preparation was completed by P.M.P.-D.; review and editing were done by M.H., M.R., J.L.E.C., and T.B.; supervision was made by M.R., T.B., and M.H.; and funding acquisition was by M.R. All authors have read and agreed to the published version of the manuscript.

Notes

The authors declare no competing financial interest.

■ ACKNOWLEDGMENTS

P.M.P.-D. thanks Secretaría de Ciencia, Humanidades, Tecnología e Innovación (SECIHTI)-México for graduate scholarship #956889 at Universidad Autónoma de Ciudad Juárez and Dirección General de Vinculación e Intercambio of UACJ for the summer 2023 international traveling stipend. This work was partially funded by SECIHTI-México under the Sistema Nacional de Investigadoras e Investigadores Fellowship program of SECIHTI CVU#222146 for 2020-2025 (M.R.). Part of this work was performed at the Center for Integrated Nanotechnologies, an Office of Science User Facility operated by the U.S. Department of Energy (DOE) Office of Science. Sandia National Laboratories is a multiprogram laboratory managed and operated by Sandia Corporation, a fully owned subsidiary of Lockheed Martin Corporation, for the U.S. Department of Energy's National Nuclear Security Administration under contract DE-AC04-94AL85000. Additional funding was provided by the Karlsruhe Nano and Micro Facility (KNMF) of the Karlsruhe Institute of Technology for the usage of APT and FIB instruments under proposal 2023-030-031793. The KNMF grants measurement time to external users for proposals pertinent to KNMF goals. Article publication charges were supported by the Institutional Open Access Program (IOAP) of the Karlsruhe Institute of Technology-Helmholtz and organized by Projekt DEAL. We thank Centro de Investigación en Materiales Avanzados-Chihuahua (CIMAV), Universidad Autónoma de Ciudad Juárez (UACJ), the Center for Integrated Nanotechnologies (CINT) of Sandia National Laboratories at Albuquerque, NM, and Karlsruhe Micro and Nano Facilities of the Karlsruhe Institute of Technology in Germany for the usage of all laboratory facilities and equipment. We thank the Programa de Movilidad at Universidad Autonóma de Ciudad Juárez (UACJ) for providing support through the summer research scholarship at the Karlsruhe Nano Micro Facility (KNMF), which was awarded to students involved in this project and greatly contributed to its success and our academic development. We also thank Dr. Oscar A. López-Galán for providing insights and comments on the main manuscript.

■ REFERENCES

(1) Falconi, C. Piezoelectric Nanotransducers. *Nano Energy* **2019**, *59*, 730−744.

(2) Caballero-Pérez, R. O.; Bravo-Castillero, J.; Pérez-Fernández, L. D.; Rodríguez-Ramos, R.; Sabina, F. J. Computation of Effective Thermo-Piezoelectric Properties of Porous Ceramics via Asymptotic Homogenization and Finite Element Methods for Energy-Harvesting Applications. *Arch. Appl. Mech.* **2020**, *90*, 1415−1429.

(3) Rupitsch, S. J.; *Piezoelectric Sensors and Actuators: Fundamentals and Applications*. Topics in Mining, Metallurgy and Materials Engineering, 1st ed.; Springer: Berlin, Heidelberg, 2019, pp. 43−77.

(4) Malik, G.; Mourya, S.; Hirpara, J. G.; Chandra, R. Surface Modification of Sputter Deposited γ-WO_3 Thin Film for Scaled Electrochromic Behaviour. *Surf. Coat. Technol.* **2019**, *375*, 708−714.

(5) Chen, P.-W.; Chang, C.-T.; Ko, T.-F.; Hsu, S.-C.; Li, K.-D.; Wu, J.-Y. Fast Response of Complementary Electrochromic Device Based on WO_3/NiO Electrodes. *Sci. Rep.* **2020**, *10* (1), 8430.

(6) Polyakov, B.; Butanovs, E.; Ogurcovs, A.; Sarakovskis, A.; Zubkins, M.; Bikse, L.; Gabrusenoks, J.; Vlassov, S.; Kuzmin, A.; Purans, J. Unraveling the Structure and Properties of Layered and Mixed ReO_3−WO_3 Thin Films Deposited by Reactive DC Magnetron Sputtering. *ACS Omega* **2022**, *7*, 1827−1837.

(7) Chang, C.-H.; Chou, T.-C.; Chen, W.-C.; Niu, J.-S.; Lin, K.-W.; Cheng, S.-Y.; Tsai, J.-H.; Liu, W. C. Study of a WO_3 Thin Film Based Hydrogen Gas Sensor Decorated with Platinum Nanoparticles. *Sens. Actuators, B* **2020**, *317*, 128145.

(8) Castillo, C.; Cabello, G.; Chornik, B.; Huentupil, Y.; Buono-Core, G. E. Characterization of Photochemically Grown Pd Loaded WO_3 Thin Films and Its Evaluation as Ammonia Gas Sensor. *J. Alloys Compd.* **2020**, *825*, 154166.

(9) Limwichean, S.; Kasayapanand, N.; Ponchio, C.; Nakajima, H.; Patthanasettakul, V.; Eiamchai, P.; Meng, G.; Horprathum, M. Morphology-Controlled Fabrication of Nanostructured WO_3 Thin Films by Magnetron Sputtering with Glancing Angle Deposition for Enhanced Efficiency Photo-Electrochemical Water Splitting. *Ceram. Int.* **2021**, *47* (24), 34455−34462.

(10) Mohamedkhair, A. K.; Drmosh, Q. A.; Qamar, M.; Yamani, Z. H. Tuning Structural Properties of WO_3 Thin Films for Photoelectrocatalytic Water Oxidation. *Catalysts* **2021**, *11* (3), 381.

(11) Li, J.-J.; Zhang, M.; Weng, B.; Chen, X.; Chen, J.; Jia, H.-P. Oxygen Vacancies Mediated Charge Separation and Collection in Pt/WO_3 Nanosheets for Enhanced Photocatalytic Performance. *Appl. Surf. Sci.* **2020**, *507*, 145133.

(12) Corby, S.; Francàs, L.; Kafizas, A.; Durrant, J. R. Determining the Role of Oxygen Vacancies in the Photoelectrocatalytic Performance of WO_3 for Water Oxidation. *Chem. Sci.* **2020**, *11*, 2907−2914.

(13) Gholami, P.; Khataee, A.; Bhatnagar, A.; Vahid, B. Synthesis of N-Doped Magnetic WO_{3-x} @Mesoporous Carbon Using a Diatom Template and Plasma Modification: Visible-Light-Driven Photocatalytic Activities. *ACS Appl. Mater. Interfaces* **2021**, *13*, 13072−13086.

(14) Shabdan, Y.; Markhabayeva, A.; Bakranov, N.; Nuraje, N. Photoactive Tungsten-Oxide Nanomaterials for Water-Splitting. *Nanomaterials* **2020**, *10*, 1871.

(15) Mineo, G.; Bruno, L.; Bruno, E.; Mirabella, S. WO_3 Nanorods Decorated with Very Small Amount of Pt for Effective Hydrogen Evolution Reaction. *Nanomaterials* **2023**, *13*, 1071.

(16) Mak, A. K.; Tuna, Ö.; Sezgin, N.; Üstün, A. M.; Yılmaz, Ş.; Öztürk, O.; Karabulut, M. Effect of Al Doping on the Electrochromic Properties of WO_3 Thin Films. *Thin Solid Films* **2022**, *751*, 139241.

(17) Kumar, A. Methods and Materials for Smart Manufacturing: Additive Manufacturing, Internet of Things, Flexible Sensors and Soft Robotics. *Manuf. Lett.* **2018**, *15*, 122−125.

(18) Zaia, E. W.; Gordon, M. P.; Yuan, P.; Urban, J. J. Progress and Perspective: Soft Thermoelectric Materials for Wearable and Internet-of-Things Applications. *Adv. Electron. Mater.* **2019**, *5* (11), 1800823.

(19) Yuan, K.; Wang, C.-Y.; Zhu, L.-Y.; Cao, Q.; Yang, J.-H.; Li, X.-X.; Huang, W.; Wang, Y.-Y.; Lu, H.-L.; Zhang, D. W. Fabrication of a Micro-Electromechanical System-Based Acetone Gas Sensor Using CeO_2 Nanodot-Decorated WO_3 Nanowires. *ACS Appl. Mater. Interfaces* **2020**, *12*, 14095−14104.

(20) Kim, Y.; Alexe, M.; Salje, E. K. H. Nanoscale Properties of Thin Twin Walls and Surface Layers in Piezoelectric WO_{3-x}. *Appl. Phys. Lett.* **2010**, *96* (3), 032904.

https://doi.org/10.1021/acsomega.4c09280
ACS Omega 2025, 10, 17249−17256

(21) Yun, S.; Song, K.; Chu, K.; Hwang, S.-Y.; Kim, G.-Y.; Seo, J.; Woo, C.-S.; Choi, S.-Y.; Yang, C.-H. Flexopiezoelectricity at Ferroelastic Domain Walls in WO_3 Films. *Nat. Commun.* **2020**, *11* (1), 4898.
(22) Pineda-Domínguez, P. M.; Boll, T.; Nogan, J.; Heilmaier, M.; Hurtado-Macías, A.; Ramos, M. The Piezoresponse in WO_3 Thin Films Due to N_2-Filled Nanovoids Enrichment by Atom Probe Tomography. *Materials* **2023**, *16*, 1387.
(23) Ramana, C. V.; Utsunomiya, S.; Ewing, R. C.; Julien, C. M.; Becker, U. Structural Stability and Phase Transitions in WO_3 Thin Films. *J. Phys. Chem. B* **2006**, *110*, 10430−10435.
(24) Vemuri, R. S.; Bharathi, K. K.; Gullapalli, S. K.; Ramana, C. V. Effect of Structure and Size on the Electrical Properties of Nanocrystalline WO $_3$ Films. *ACS Appl. Mater. Interfaces* **2010**, *2*, 2623−2628.
(25) Enriquez-Carrejo, J. L.; Ramos, M. A.; Mireles-Jr-Garcia, J.; Hurtado-Macias, A. Nano-Mechanical and Structural Study of WO_3 Thin Films. *Thin Solid Films* **2016**, *606*, 148−154.
(26) Vemuri, R. S.; Carbjal-Franco, G.; Ferrer, D. A.; Engelhard, M. H.; Ramana, C. V. Physical Properties and Surface/Interface Analysis of Nanocrystalline WO_3 Films Grown under Variable Oxygen Gas Flow Rates. *Appl. Surf. Sci.* **2012**, *259*, 172−177.
(27) Gullapalli, S. K.; Vemuri, R. S.; Manciu, F. S.; Enriquez, J. L.; Ramana, C. V. Tungsten Oxide (WO_3) Thin Films for Application in Advanced Energy Systems. *J. Vac. Sci. Technol.* **2010**, *28*, 824−828.
(28) Peng, Y.; Han, G.; Liu, F.; Xiao, W.; Liu, Y.; Zhong, N.; Duan, C.; Feng, Z.; Dong, H.; Hao, Y. Ferroelectric-like Behavior Originating from Oxygen Vacancy Dipoles in Amorphous Film for Non-Volatile Memory. *Nanoscale Res. Lett.* **2020**, *15* (1), 134.
(29) Kavitha, V. S.; Reshmi Krishnan, R.; Sreeja Sreedharan, R.; Suresh, K.; Jayasankar, C. K.; Mahadevan Pillai, V. P. Tb^{3+}-Doped WO_3 Thin Films: A Potential Candidate in White Light Emitting Devices. *J. Alloys Compd.* **2019**, *788*, 429−445.
(30) Mansouri, M.; Mahmoodi, T. Ab Initio Investigation on the Effect of Transition Metals Doping and Vacancies in WO_3. *Acta Phys. Pol., A* **2016**, *129*, 8.
(31) Wang, X.; Huan, Y.; Ji, S.; Zhu, Y.; Wei, T.; Cheng, Z. Ultra-High Piezoelectric Performance by Rational Tuning of Heterovalent-Ion Doping in Lead-Free Piezoelectric Ceramics. *Nano Energy* **2022**, *101*, 107580.
(32) Yoo, S.-H.; Kim, S.-H.; Woods, E.; Gault, B.; Todorova, M.; Neugebauer, J. Origins of the Hydrogen Signal in Atom Probe Tomography: Case Studies of Alkali and Noble Metals. *New J. Phys.* **2022**, *24*, 013008.
(33) Kühbach, M.; Bajaj, P.; Celik, M. H.; Jägle, E. A.; Gault, B. On Strong Scaling and Open-Source Tools for Analyzing Atom Probe Tomography Data. *arXiv*, **2020**. .
(34) Gault, B. A Brief Overview of Atom Probe Tomography Research. *Appl. Microsc.* **2016**, *46*, 117.
(35) Soergel, E. Piezoresponse Force Microscopy (PFM). *J. Phys. D: Appl. Phys.* **2011**, *44*, 464003.
(36) Qiao, H.; Kwon, O.; Kim, Y. Electrostatic Effect on Off-Field Ferroelectric Hysteresis Loop in Piezoresponse Force Microscopy. *Appl. Phys. Lett.* **2020**, *116* (17), 172901.
(37) Cullity, B. D.; *Elements of X-Ray Diffraction*. Addison-Wesley series in metallurgy and materials, 2nd ed.; Addison-Wesley Pub. Co.: Reading, Mass, 1978, pp. 281−528.
(38) Liang, Y.-C.; Chang, C.-W. Preparation of Orthorhombic WO_3 Thin Films and Their Crystal Quality-Dependent Dye Photodegradation Ability. *Coatings* **2019**, *9*, 90.
(39) Brüger, A.; Fafilek, G.; Neumann-Spallart, M. Identification of Different WO_3 Modifications in Thin Films for Photocatalytic Applications by Peak Shape Analysis in High Temperature XRD Diffractometry. *J. Photochem. Photobiol., A* **2024**, *457*, 115879.
(40) Fan, X.; Liu, C.; Gao, B.; Li, H.; Zhang, Y.; Zhang, H.; Gao, Q.; Cao, X.; Tang, Y. Electronic Structure Engineering of Pt Species over Pt/WO_3 toward Highly Efficient Electrocatalytic Hydrogen Evolution. *Small* **2023**, *19* (32), 2301178.
(41) Eusterholz, M. K.; Boll, T.; Ott, V.; Stüber, M.; Lu, Y.; Gebauer, J.; Ulrich, S.; Kauffmann, A.; Heilmaier, M. Nanoscale Oxide Formation at α-Al 2 O 3 −Nb Interfaces. *Adv. Eng. Mater.* **2023**, *25* (14), 2201441.
(42) Billah, M.; Terasawa, Y.; Masud, M. K.; Asahi, T.; Hegazy, M. B. Z.; Nagata, T.; Chikyow, T.; Uesugi, F.; Hossain, M. S. A.; Yamauchi, Y. Giant Piezoresponse in Nanoporous (Ba,Ca)(Ti,Zr)O_3 Thin Film. *Chem. Sci.* **2024**, *15*, 9147−9154.
(43) Kim, D. B.; Kim, J. Y.; Han, J.; Cho, Y. S. Strain Engineering in Power-Generating and Self-Powered Nanodevices. *Nano Energy* **2024**, *125*, 109551.

https://doi.org/10.1021/acsomega.4c09280
ACS Omega 2025, 10, 17249−17256